RSC Advances

PAPER

View Article Online
View Journal | View Issue

Cite this: *RSC Adv.*, 2022, **12**, 13281

Role of metal and anions in organo-metal halide perovskites $CH_3NH_3MX_3$ (M: Cu, Zn, Ga, Ge, Sn, Pb; X: Cl, Br, I) on structural and optoelectronic properties for photovoltaic applications†

Maliha Nishat, *[a] Md. Kamal Hossain, [b] Md. Rakib Hossain, [c] Shamima Khanom,[b] Farid Ahmed[b] and Md. Abul Hossain[b]

Received 22nd November 2021
Accepted 7th April 2022

DOI: 10.1039/d1ra08561a

rsc.li/rsc-advances

Methylammonium metal halide perovskites have recently been explored for new uses due to their unique and exciting optoelectronic properties. Their exceptional electronic properties have often been attributed to the overlap between the metal cation s and halogen p states. In this study, density functional theory calculations have been carried out based on the orthorhombic phase of the organometal trihalide perovskite $CH_3NH_3MX_3$ (M: Cu, Zn, Ga, Ge, Sn, Pb; X: Cl, Br, I) to systematically investigate the effects of the metal cation and halogen anion on the structural, electronic, and optical properties for solar cell applications. The calculated lattice parameters agree well with previously obtained experimental and theoretical results. All of these perovskites are direct band gap compounds at the G symmetry point, except $CH_3NH_3GaX_3$. The band gap increases from iodide to chloride and also with the metal cation size, from Ge to Pb or Cu to Zn. Furthermore, metal halide perovskites show blue shifts in their optical absorption spectra with an increase in metal cation size. Among the studied examples, $CH_3NH_3GaBr_3$ and $CH_3NH_3CuCl_3$ absorb a wide range of light, from UV to the visible region, and possess very unusual high dielectric constants and refractive indices. Our calculations reveal that $CH_3NH_3SnI_3$, $CH_3NH_3GeI_3$, and $CH_3NH_3ZnI_3$ are favorable candidates for lead-free photovoltaic applications.

1 Introduction

In recent years, perovskite-based photovoltaics (PVs) have received tremendous interest, especially when they implement a metal halide perovskite as an absorber material in a hybrid solar cell. The general formula of a halide perovskite compound is ABX_3; where the 'A-site' involves a large (natural) cation, the 'B-site' is filled with considerably divalent metal cations and the 'X-site' contains a halide anion. The very first metal halide perovskite to be distinguished was $CH_3NH_3PbI_3$ by Weber.[1] In 2009, Miyasaka and his coworkers[2] disclosed it as a remarkable light sensitizer which attracted huge research interest to $CH_3NH_3PbI_3$. In a couple of years, it showed a tremendous increase in power conversion efficiency (PCE) from 3.8% (in 2009) to more than 22%.[3,4] Thus the growth in the field of metal halide perovskites is due to their outstanding optoelectronic properties, including superb charge carrier mobility, long diffusion length, high optical absorption coefficient, tunable band gaps and cheap production cost. So, they have become favorable materials that can easily fit in many other optoelectronic devices like lasers, light-emitting diodes (LED), photo-detectors and field-effect transistors (FETs).[5,6] Moreover, because of their natural abundance, these materials result in cheaper and more efficient solar cells than silicon-based photovoltaics.[7] In addition, a wide range of diverse processing technologies (like vacuum-based solution techniques and low-temperature solution processes) can be implemented to prepare metal halide perovskites, making them very fascinating.[8–10]

The crystal structure of $CH_3NH_3PbX_3$ is found to be very responsive to temperature.[11,12] $CH_3NH_3PbX_3$ holds a cubic phase at high temperature, and as the temperature decreases, it transforms into a tetragonal phase and becomes orthorhombic at lower temperature.[11–14] Recently orthorhombic $CH_3NH_3PbI_3$ was determined with its organic CH_3NH_3 part.[11] Many theoretical and experimental investigations have been reported on orthorhombic perovskite $CH_3NH_3PbI_3$.[15–18] Besides, the A, B and X-sites in ABX_3-type perovskites can be altered or tuned to improve their performance in perovskite-based photovoltaic devices.

The most famous high-PCE perovskite material has Pb in it, and it is toxic, which is undesirable, and chemically unstable

[a]Department of Physics, Pabna University of Science and Technology, Pabna-6600, Bangladesh. E-mail: malihanishat@pust.ac.bd
[b]Department of Physics, Jahangirnagar University, Dh, aka-1342, Bangladesh
[c]Department of Physics, Bangabandhu Sheikh Mujibur Rahman Science and Technology University, Gopalganj-8100, Bangladesh

† Electronic supplementary information (ESI) available. See https://doi.org/10.1039/d1ra08561a

under ambient conditions.[19] Hence, lead needs to be replaced for the wider commercialization and application of this type of compound in the photovoltaic and optoelectronic sectors. In this regard, Sn is one of the realistic and possible elements to replace Pb in $CH_3NH_3PbI_3$ structures as it comes from the same IVA subgroup.[19,20] Many experimental and theoretical investigations have been done on Sn-based perovskite systems.[19,21,22] Tin is highly sensitive to air, which quickly changes the oxidization state from Sn^{2+} to Sn^{4+}. This is one of the reasons why Sn-based perovskite have a small PCE while lead-based perovskites possess a high PCE. Ge belongs to group IVA (the same subgroup as Pb and Sn) and Ge-based perovskite shows a comparable optical absorption to Pb-based perovskite.[23] Furthermore, it was experimentally confirmed that cation size affects the crystallographic features of Ge-perovskites.[24] Thus Ge-based perovskites are an alternative nontoxic choice for photovoltaic material, which is confirmed by research. Both Sn and Ge possess similar chemical composition and valences to Pb as they belong to the same subgroup in the periodic table. So, they can easily replace Pb. Also it is very crucial to analyze the bonding nature of lone-pair electrons[25] on these metals (Pb-6s2, Sn-5s2 & Ge-4s2) because they have a vital influence on the electronic properties of these metal-based perovskites.

These days, lead can be supplanted in perovskites with reasonable, alternative, environmentally friendly, earth-abundant elements like transition metals, which may be important in terms of PCE. Pb replacement with transition metals like Cu, Zn or Ga can make novel nontoxic and clean perovskites for solar cells, which can also show an improvement in photovoltaic solar cells. Previously two-dimensional layered copper perovskites were implemented as absorber materials and attained low PCE values (0.51 and 0.63%, respectively).[26] Perovskite-based photovoltaics with the suitable addition of Zn^{2+} can improve the regular PCE from 12.1% to 16.3%, which was reported experimentally.[27]

In the present work, we perform a systematic simulation on a series of orthorhombic metal halide perovskites to investigate their size (metal cation and halide anion) dependent properties by implementing first-principles density functional theory (DFT) calculations. We took $CH_3NH_3PbI_3$ as a primary model and then replaced the I^- anion with Br^- and Cl^- anions to make $CH_3NH_3PbX_3$ compounds where X: Cl, Br, I. A further metal (Pb) cation was also replaced in $CH_3NH_3PbX_3$ with a sequence of transition metal and post transition metal cations to make $CH_3NH_3MX_3$ systems where M: Cu, Zn, Ga, Ge, Sn, Pb. The crystal configuration, electronic parameters, optical properties, and the structure–property relationships were explored for all of these perovskite compounds. The essential concern of this study is to understand the size effect of the metal cation and halide anion on the optoelectronic properties of these perovskite compounds. Also, the chemistry of lone pairs of the metal cations and halide anions is a key point for analysis of their impact on the electronic structure and characteristics of these compounds. Further, a proper understanding of the optical parameters is crucial so they can be used in solar cells and other optoelectronic devices like diodes, lasers, *etc.*

2 Computational details

In this work, *ab initio* calculations were performed for orthorhombic $CH_3NH_3MX_3$ by using the framework of density functional theory[28] embedded in Cambridge Sequential Total Energy (CASTEP) code[29] where the Kohn–Sham equations get solved. The wave functions of the valence electrons are expanded in a basis set of plane waves. Ultra-soft pseudo-potentials can represent the existence of a tightly-bound core electron, and they define the interaction between electron and ion.[30] The exchange–correlation potential is treated within the Perdew–Burke–Ernzerhof (1996) version of the generalized gradient approximation (PBE-GGA).[31] While Ceperley and Alder developed the local density approximation (LDA), Perdew and Zunger parameterized it.[32,33]

For geometric optimization, a $2 \times 3 \times 2$ Monkhorst–Pack grid[34] was employed in the Brillouin zone of the unit cell to produce a uniform grid of k-points along the three axes in reciprocal space. The kinetic cut-off energy was chosen at 280 eV for $CH_3NH_3GeX_3$, $CH_3NH_3SnX_3$ and $CH_3NH_3PbX_3$ (same-group) compounds, whereas it was 400 eV for $CH_3NH_3CuX_3$, $CH_3NH_3ZnX_3$ and $CH_3NH_3GaX_3$ (same-period) compounds. All of the structures become relaxed in their optimized geometry. The structural parameters of $CH_3NH_3MX_3$ (*Pnma* (no: 62) space group) were calculated using the BFGS (Broyden–Fletcher–Goldfarb–Shanno) technique, where the following parameters are taken to obtain a converged geometry: stress 0.1 GPa, residual force 0.05 eV $Å^{-1}$ and energy change per atom less than 2×10^{-5} eV. Optical parameters such as absorption coefficient $\alpha(\omega)$, refractive index $n(\omega)$, optical conductivity $\sigma(\omega)$, optical reflectivity $R(\omega)$ and energy-loss spectrum $L(\omega)$ can be calculated by utilizing the complex dielectric function: $\varepsilon(\omega) = \varepsilon_1(\omega) + i\varepsilon_2(\omega)$.

3 Results and discussion

3.1 Geometry optimization

Accurate structural understandings are essential for the better prediction of the optoelectronic characteristics of perovskites. ABX_3-type perovskites are sensitive to temperature and change their phase with temperature.[11,12] In the present studies, we concentrate on the orthorhombic phase, which is thermodynamically stable, and this is additionally suitable for DFT estimation at zero temperature.[35] The optimized unit cell of $CH_3NH_3MX_3$ (M: Cu, Zn, Ga, Ge, Sn, Pb; X: Cl, Br, I) in the orthorhombic phase is pictured in Fig. 1. A total of eighteen compounds are fully optimized and relaxed in their ground state. This orthorhombic perovskite structure forms with octahedral $[BX_6]$ cations that share a corner of the net with halide anions and organic methylammonium $[CH_3NH_3]^+$ cations situated within the octahedral network.

To quantitatively depict the crystal structure, a parameter called the tolerance factor was calculated to define the crystal stability with variations in metal cations and halide anions. It also defines the stability of the perovskite material in solar cells. Analogous to Goldschmidt's early method, the tolerance factors of hybrid organic–inorganic perovskites are calculated with (effective) ionic radii by using the general formula:[36]

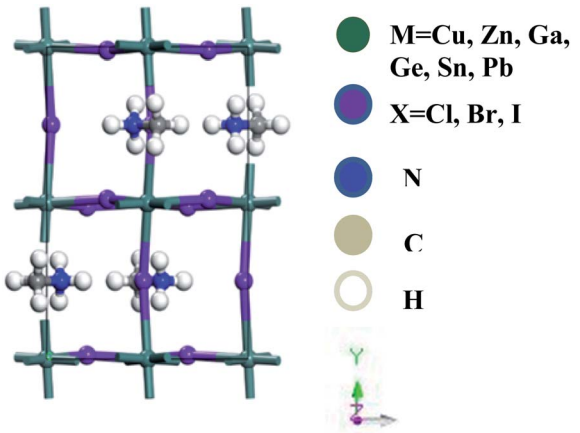

Fig. 1 A lattice structural representation of the organometal trihalide perovskite $CH_3NH_3MX_3$ (M: Cu, Zn, Ga, Ge, Sn, Pb; X: Cl, Br, I) in the orthorhombic phase.

$$\text{Tolerance factor} = \left(r_{A(\text{eff.})} + r_X\right) \Big/ \sqrt{2}(r_B + r_X) \quad (1)$$

where, $r_{A(\text{eff.})}$ is the effective ionic radius of the organic A cation, r_X is the ionic radius of the halide X anion and r_B is the ionic radius of the divalent metal ion B in an ABX_3 kind of perovskite. Using an ionic radius for organic cations is puzzling,[37] so a semi-empirical approach was chosen which leads to a reliable value of effective ionic radii for organic cations.[38]

This effective ionic radius of the organic cation was used to modify Goldschmidt's initial approach to calculate the tolerance factor. To calculate the tolerance factors presented in Table 1, the effective radii of the $[CH_3NH_3]^+$ (methylammonium, 217 pm) were used from ref. 38 and Shannon's ionic radii[37] were used for metal cations and halide anions. Another stability parameter is the octahedral factor μ, which is defined by the ratio r_B/r_X. Both the tolerance factor and the μ parameter can give information about the stability of perovskites within the range of $\mu > 0.41$ and $0.76 <$ tolerance factor < 1.13.[38–41] Most cubic perovskites are formed in the TF range of 0.8–1.0, while a distorted octahedral perovskite TF lies in 0.76–0.90.[40] Besides, a TF larger than one forms highly distorted perovskites, and TF > 1.13 results in layered structures with face-sharing octahedra.[40] Our calculations found that $CH_3NH_3PbX_3$ and $CH_3NH_3SnX_3$ have TF in the range of 0.904–0.938, while $CH_3NH_3GeX_3$, $CH_3NH_3ZnX_3$, $CH_3NH_3CuX_3$ and $CH_3NH_3GaI_3$ have TF larger than 1 but less than 1.13, which results in distorted perovskites. However, $CH_3NH_3GaBr_3$ and $CH_3NH_3GaCl_3$ have TF larger than 1.13, making them non-perovskites but still useful for optoelectronic device applications. It is observed from Table 1 that with an increase in halide size (from Cl to I), both the tolerance factor and μ decrease gradually for all compounds, indicating the stability of the perovskites. On the other hand, with an increase in metal cation size in the same period (from Cu → Zn → Ga) and the same group (Ge → Sn → Pb), the same thing happened (except for $CH_3NH_3GaX_3$), which may be due to structural distortion. According to the limit of tolerance factor and μ, all of the studied compounds can form stable 3D perovskites except $CH_3NH_3GaX_3$. The exceptions may be non-perovskites and can be used in other optoelectronic sectors. Fig. 2 displays a structural map of our studied compounds. The areas surrounded by the dotted lines (black and red) represent the boundary limits for the formation of stable perovskites, and the compounds that lie in those areas can form perovskites.

Determining the DFT lattice constant was essential for assessing other parameters. Therefore, the obtained values and other available lattice constant and cell volume values from the literature for all of the perovskite compounds are tabulated in Table 2, based on the use of two different functionals. Generally,

Table 1 A list of tolerance factors, octahedral factors (μ) and formation of enthalpy values (ΔH_f) (in units of kJ mol^{-1}) for $CH_3NH_3MX_3$

Material	Tolerance factor	μ	ΔH_f
$CH_3NH_3CuCl_3$	1.108	0.403	−205.329
$CH_3NH_3ZnCl_3$	1.104	0.409	−194.149
$CH_3NH_3GaCl_3$	1.158	0.343	−101.868
$CH_3NH_3GeCl_3$	1.108	0.403	−264.494
$CH_3NH_3SnCl_3$	0.929	0.674	−265.276
$CH_3NH_3PbCl_3$	0.938	0.657	−134.925
$CH_3NH_3CuBr_3$	1.086	0.372	−59.736
$CH_3NH_3ZnBr_3$	1.082	0.378	−61.989
$CH_3NH_3GaBr_3$	1.132	0.316	−195.846
$CH_3NH_3GeBr_3$	1.086	0.372	−56.023
$CH_3NH_3SnBr_3$	0.918	0.622	−55.433
$CH_3NH_3PbBr_3$	0.927	0.607	−159.599
$CH_3NH_3CuI_3$	1.055	0.332	−51.256
$CH_3NH_3ZnI_3$	1.051	0.336	−53.492
$CH_3NH_3GaI_3$	1.096	0.282	−187.365
$CH_3NH_3GeI_3$	1.055	0.332	−47.537
$CH_3NH_3SnI_3$	0.904	0.555	−46.941
$CH_3NH_3PbI_3$	0.912	0.541	−169.99

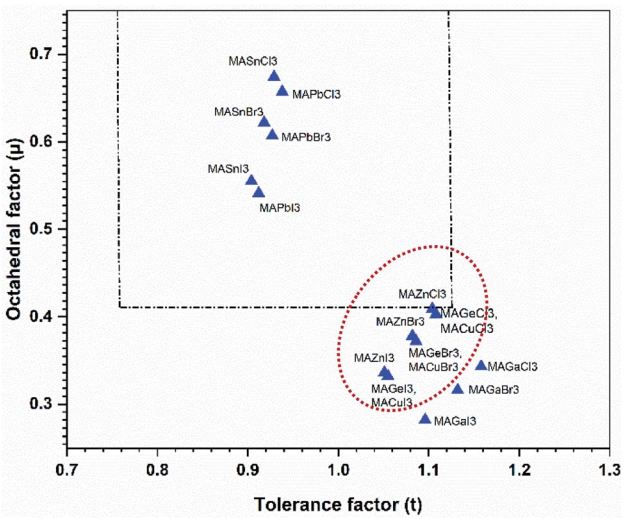

Fig. 2 A structural map of $CH_3NH_3MX_3$ compounds. The dotted lines are the boundary lines mentioned in the text. Compounds in the red dotted circle represent stable perovskites.

the value of lattice parameters shows underestimates for LDA and overestimates for GGA.

However, in Table 2, both LDA and GGA overestimate the experimental results. This finding is consistent with the outcomes for traditional semiconductors. However, $CH_3NH_3MCl_3$ shows overestimated values of the lattice parameters for both LDA (CAPZ) and GGA(PBE) functionals, and this may be due to the lack of van der Waals interactions between the organic part (CH_3NH_3) and the octahedral [M–Cl] corner.[50] If one considers dispersive interactions in a specific form, the obtained lattice parameters can agree well with the experimental data.[49,50] On account of the DFT result, the experimental

Table 2 Optimized lattice parameters and cell volumes of $CH_3NH_3MX_3$ (M: Cu, Zn, Ga, Ge, Sn, Pb; X: Cl, Br, I) perovskites obtained using the two functionals LDA-CAPZ and GGA-PBE, and a comparison with other available studies (both experimental and theoretical)

		Lattice parameter (Å)				
Material	Method	*a*	*b*	*c*	Volume (Å^3)	Ref.
$CH_3NH_3CuCl_3$	LDA-CAPZ	14.749	9.204	9.599	1303.062	—
	GGA-PBE	14.945	9.139	9.609	1314.088	—
	Experiment	18.8	4.23	11.11	875	42
$CH_3NH_3ZnCl_3$	LDA-CAPZ	12.735	7.374	12.651	1188.029	—
	GGA-PBE	13.453	7.870	14.935	1581.245	—
$CH_3NH_3GaCl_3$	LDA-CAPZ	11.371	9.898	10.010	1126.620	—
	GGA-PBE	11.480	11.610	11.545	1538.830	—
$CH_3NH_3GeCl_3$	LDA-CAPZ	14.749	9.204	9.599	1303.062	—
	GGA-PBE	14.945	9.139	9.609	1314.088	—
	Theory	7.28	7.28	10.61	487.54	43
$CH_3NH_3SnCl_3$	LDA-CAPZ	12.729	11.383	11.494	1665.414	—
	GGA-PBE	11.555	11.327	11.677	1528.326	—
	Experiment		5.76		—	43
$CH_3NH_3PbCl_3$	LDA-CAPZ	10.990	11.263	11.124	1376.933	—
	GGA-PBE	11.469	11.616	11.589	1543.932	—
	Experiment	8.020	—	11.260	—	44
	Theory	7.850	8.220	11.150	719.476	—
$CH_3NH_3CuBr_3$	LDA-CAPZ	7.470	9.922	8.321	616.752	—
	GGA-PBE	9.569	10.305	8.729	860.989	—
$CH_3NH_3ZnBr_3$	LDA-CAPZ	7.313	10.861	8.229	653.603	—
	GGA-PBE	8.101	11.037	10.334	923.996	—
$CH_3NH_3GaBr_3$	LDA-CAPZ	7.272	11.691	7.870	669.026	—
	GGA-PBE	7.783	11.382	8.309	736.073	—
$CH_3NH_3GeBr_3$	LDA-CAPZ	7.459	10.849	8.041	650.687	—
	GGA-PBE	7.842	11.485	8.449	760.919	—
	Theory	7.64	7.64	10.91	552.01	24
$CH_3NH_3SnBr_3$	LDA-CAPZ	8.089	12.324	8.728	870.029	—
	GGA-PBE	8.0853	12.331	8.721	869.50	—
	Experiment		5.89		—	45
$CH_3NH_3PbBr_3$	LDA-CAPZ	7.663	11.713	8.665	777.709	—
	GGA-PBE	8.183	12.314	8.963	903.161	—
	Experiment	7.94	11.85	8.59	808.73	46
	Theory	7.95	12.01	8.67	830.67	46
$CH_3NH_3CuI_3$	LDA-CAPZ	8.106	11.383	11.494	732.679	—
	GGA-PBE	8.695	11.214	9.237	900.660	—
$CH_3NH_3ZnI_3$	LDA-CAPZ	8.010	11.229	7.946	830.815	—
	GGA-PBE	8.452	12.411	9.821	1030.201	—
$CH_3NH_3GaI_3$	LDA-CAPZ	8.080	12.022	8.116	788.305	—
	GGA-PBE	8.572	11.966	8.913	914.136	—
$CH_3NH_3GeI_3$	LDA-CAPZ	8.265	11.442	8.404	749.742	—
	GGA-PBE	8.683	12.349	8.769	940.184	—
	Experiment	8.553	8.553	11.162	707.2	24
	Theory	8.20	8.20	11.34	806.58	24
$CH_3NH_3SnI_3$	LDA-CAPZ	8.128	12.071	8.850	868.301	—
	GGA-PBE	8.917	12.670	9.206	1040.079	—
	Theory	8.556	12.428	8.326	885.400	47
$CH_3NH_3PbI_3$	LDA-CAPZ	8.176	12.442	8.971	912.582	—
	GGA-PBE	8.992	13.068	9.297	1092.467	—
	Experiment ($T = 100$ K)	8.866	12.629	8.577	960.338	48
	Experiment ($T = 100$ K)	8.836	12.580	8.555	951.010	11
	Theory	9.226	12.876	8.619	1023.880	49

lattice constant was not utilized. The over-restrictive issues in DFT brought about underestimated self-interaction between the charges, which is why the theoretical result becomes smaller than the experimental data. So, our calculated structural parameters are in the acceptable range. In this way, the contrasts between our outcomes and the trial information are as anticipated.

Our obtained lattice parameters also agree well with other theoretical results. It is also observed from Fig. 3 that the cell volume decreases with an increase in the anion size (from Cl to I). Thus the cell volume and the radius of the halide anion share an inverse relationship, while a proportional increase has been shown for the radius of the metal cation. The radius of the metal cation increases from Ge to Pb (same group) and from Cu to Ga (same period), so the lattice of the structure is additionally increasing with a specific end goal of upholding the structural symmetry. According to Fig. 3, the cell volumes of all the perovskites increase with the size of the metal cation (except $CH_3NH_3GaX_3$).

The calculated bond lengths are given in Table 3, and this leads to knowledge of the structural alignments and energy gaps of the perovskites. We refer to the six M–X (metal–halide) bond lengths of the MX_6 octahedra and other important bonds to observe the variations among the eighteen perovskite compounds. Metal cation and halide anion share six bonds; four bonds are located in the equatorial plane, and the other two bonds are in the axial direction. Interestingly, the M–X bonds are shorter when the atomic size decreases in the same group (from Ga to Cu) and the same period (Pb to Ge). Therefore, all the bond lengths are larger in the equatorial direction than in the axial direction. From Table 3, it is also observed that C–H bond lengths are more significant than the N–H bond length in $CH_3NH_3MX_3$. As nitrogen has more valence electrons than carbon, it attracts the positively ionized hydrogen atom more strongly and makes a firm bond with it. Also, the N–H ion possesses a larger dipole moment than the C–H ion, which is why the N–H ion is more strongly pulled towards the halogen atoms by the van der Waals forces.

Moreover, it is well known that the enthalpy of formation is an essential tool for determining the thermodynamic stability of a material.[51,52] Previous studies reported the standard enthalpy of formation of hybrid organic–inorganic perovskites from the corresponding crystalline CH_3NH_3X and PbX_2 salts which form $CH_3NH_3PbX_3$ and it can be written as:

$$CH_3NH_3X_{(s)} + PbX_{2(s)} \rightarrow CH_3NH_3PbX_{3(s)}, \Delta H_f$$

Here ΔH_f can be calculated with the help of the following equations:

$$\Delta H_f = \Delta H_f(\text{products}) - \Delta H_f(\text{reactants})$$
$$= \Delta H_f(CH_3NH_3PbX_3) - \left(\Delta H_f(CH_3NH_3X) + \Delta H_f(PbX_2)\right)$$

Our calculated formation enthalpies are tabulated in Table 1 and they exhibit negative values for all the compounds, confirming their thermodynamic stability. Besides, the ΔH_f values of $CH_3NH_3PbX_3$ are quite comparable with other theoretical studies.[53,54]

3.2 Electronic properties

Investigating electronic properties is very important for metal halide perovskites to determine their various prospective applications. In this regard, we have calculated the band structure, density of states (DOS) and projected/partial density of states (PDOS) of orthorhombic $CH_3NH_3MX_3$ by using the DFT-GGA (PBE) and LDA (CAPZ) level of theory. All calculated band diagrams in the high symmetry zone are depicted in Fig. 4 for $CH_3NH_3MX_3$ compounds.

In the band structures, all energies are relative to the Fermi level, and the top of the valence band indicates the Fermi level for semiconductors. Here it is observed that all the perovskites possess a direct band gap at the G symmetry point except $CH_3NH_3GaX_3$. All the B-site metal cations (Cu, Zn, Ga, Ge, Sn and Pb) have fully or partially filled valence 3s, 4s, 5s and 6s orbitals, respectively, and these are located under the upper

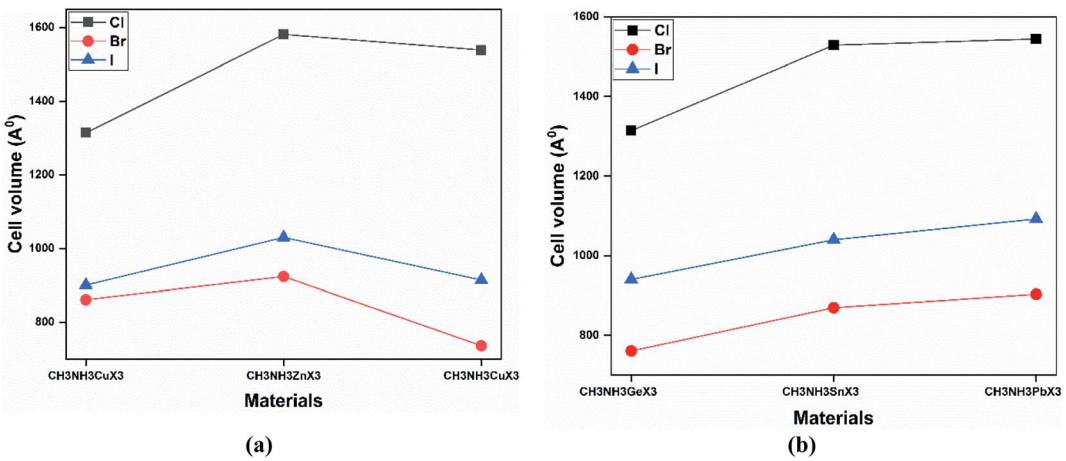

Fig. 3 A comparison of the cell volume (in Å) values upon varying the metal and halide at the GGA-PBE level of theory for (a) same-period and (b) same-group perovskite compounds.

Table 3 Bond lengths in angstrom (Å) for $CH_3NH_3MX_3$ structures using the GGA-PBE level of theory

Material	Bond length (Å)												
	Equatorial plane									Axial plane			
	M–X1	M–X2	M–X3	M–X4	N–C	N–H1	N–H2	C–H1	C–H2	M–X5	M–X6	N–H3	C–H3
$CH_3NH_3CuCl_3$	2.33	2.33	2.45	2.41	1.49	1.05	1.05	1.09	1.09	2.39	2.42	1.05	1.09
$CH_3NH_3ZnCl_3$	2.22	2.22	2.30	2.30	1.49	1.05	1.04	1.09	1.09	2.40	2.40	1.05	1.10
$CH_3NH_3GaCl_3$	2.37	2.37	2.36	2.36	1.46	1.06	1.05	1.10	1.10	2.51	2.50	1.05	1.10
$CH_3NH_3GeCl_3$	2.33	2.33	4.43	2.37	1.51	1.04	1.04	1.10	1.09	2.70	2.83	1.04	1.09
$CH_3NH_3SnCl_3$	2.83	2.83	2.98	2.98	1.49	1.05	1.04	1.09	1.09	2.93	2.91	1.04	1.09
$CH_3NH_3PbCl_3$	2.91	2.83	2.83	2.90	1.49	1.05	1.05	1.09	1.09	2.93	2.91	1.05	1.09
$CH_3NH_3CuBr_3$	2.32	4.16	4.16	2.32	1.49	1.05	1.05	1.09	1.09	2.58	2.58	1.05	1.09
$CH_3NH_3ZnBr_3$	2.32	4.30	4.30	2.32	1.49	1.06	1.04	1.09	1.09	2.94	2.94	1.04	1.09
$CH_3NH_3GaBr_3$	2.75	2.97	2.75	2.75	1.49	1.05	1.04	1.09	1.09	2.85	2.85	1.04	1.09
$CH_3NH_3GeBr_3$	2.86	2.98	2.98	2.86	1.50	1.04	1.04	1.09	1.09	2.88	2.88	1.04	1.09
$CH_3NH_3SnBr_3$	3.03	3.04	3.04	3.03	1.50	1.05	1.04	1.10	1.09	3.10	3.10	1.04	1.09
$CH_3NH_3PbBr_3$	3.29	3.29	3.29	3.29	1.51	1.04	1.04	1.09	1.09	3.12	3.12	1.04	1.09
$CH_3NH_3CuI_3$	2.54	3.83	3.83	2.54	1.49	1.05	1.04	1.09	1.09	2.81	2.81	1.04	1.09
$CH_3NH_3ZnI_3$	2.56	3.95	3.95	2.56	1.49	1.06	1.04	1.09	1.10	3.11	3.11	1.04	1.10
$CH_3NH_3GaI_3$	3.09	3.12	3.12	3.09	1.49	1.05	1.04	1.09	1.09	3.01	3.01	1.04	1.09
$CH_3NH_3GeI_3$	3.16	3.18	3.18	3.16	1.50	1.04	1.04	1.09	1.09	3.11	3.11	1.04	1.09
$CH_3NH_3SnI_3$	3.06	3.08	3.08	3.06	1.50	1.05	1.03	1.09	1.09	3.06	3.06	1.03	1.09
$CH_3NH_3PbI_3$	3.30	3.34	3.34	3.30	1.50	1.05	1.04	1.09	1.09	3.29	3.29	1.04	1.09

portion of the valence bands (VB) and thus these lone pairs are mainly responsible for the formation of valence band maxima (VBM). Lone-pair electrons directly affect the electronic structure of these metal halide perovskites. If the A-site CH_3NH_3 cation and X-site halogen anion (for example, iodine, I) are kept fixed and variation is made at the B-site metal, then it is noticed that the increase in the level of lone-pair states ($4s^1$[Cu], $4s^2$ [Zn], $4s^2$ [Ge], $5s^2$ [Sn], $6s^2$ [Pb]) leads to wider bandgaps for these perovskites. The same thing happened for fixing the X-site as Br^- or Cl^- anions. Now let us keep the A-site CH_3NH_3 cation and any metal cation (M: Cu, Zn, Ge, Sn, Pb) fixed and observe variation at the X-site (X: Cl, Br, I). Then we see the reverse case. With an increase in the level of the lone-pair states ($3s^2$[Cl], $4s^2$[Br], $5s^2$[I]) of the halide anion, the width of the bandgaps gradually decreased for the studied compounds. The unfilled s-orbitals or lone-pair electrons of these metal cations can introduce unfamiliar properties.[55] Herein for all the structures, both the conduction band minima (CBM) and the valence band maxima are isotropic and dispersive (*i.e.*, with a large bandwidths), which indicates minor carrier effective masses and this is useful in photovoltaic sectors. In all the structures, the fluctuations of the bottom conduction band (CB) are more substantial, indicating a quicker passage of photoelectrons. Also, the top VB and bottom CB are broad, which implies non-localized states and long-distance transport of excitons in these materials.

According to Fig. 4, if the halide changes from Cl to I, then the CB and VB, especially an inferior VB, are shifted to the Fermi level. It is also same for metal variation (from Ge to Pb and from Cu to Zn). This happens because the number of lone-pair electrons increases, which lead to more states and bands near the Fermi level.

All the calculated fundamental bandgaps at G symmetry points and other available theoretical and experimental values are listed in Table 4. From Table 4, we observe that as the halide changes from Cl to I, the bandgap decreases, and it increases with atomic radius in the same group (Ge to Pb) and in the same period (Cu to Zn). Also, the $CH_3NH_3GeX_3$ band gaps are quite close to those of $CH_3NH_3PbX_3$ and larger than those of $CH_3NH_3SnX_3$, as clearly depicted in Fig. 4. This makes $CH_3NH_3GeX_3$ a favorable candidate for solar cell applications. Further $CH_3NH_3ZnX_3$ also possesses a band gap that is quite close to $CH_3NH_3PbX_3$ and the band gap of $CH_3NH_3ZnI_3$ is (1.547 eV) very close to that of $CH_3NH_3PbI_3$ (1.761 eV). This is also a good sign for their application in solar cells. $CH_3NH_3GaX_3$ show metallic nature, which introduces a new idea for implementing them in other metallic/optoelectronic applications as they are non-perovskite compounds. With a decrease in atomic radius at the B-site, the nucleus gradually increases its electrostatic force on valence electrons. So, the nucleus strongly grasps the valence electrons which lowers the band gap and bonding energy in these materials. This may be one of the reasons why the band gap decreases with a reduction in atomic size. Our calculated band gap is closer to and comparable with experimental results. This trend has furthermore been witnessed in different studies on same-group compounds ($CH_3NH_3GeX_3$, $CH_3NH_3SnX_3$, $CH_3NH_3PbX_3$).[58] An exception has been observed for the experimental value of $CH_3NH_3CuCl_3$ as very little work has been done on it. Also, experiments have been done on different phases and temperatures, which also caused the variation in our calculated

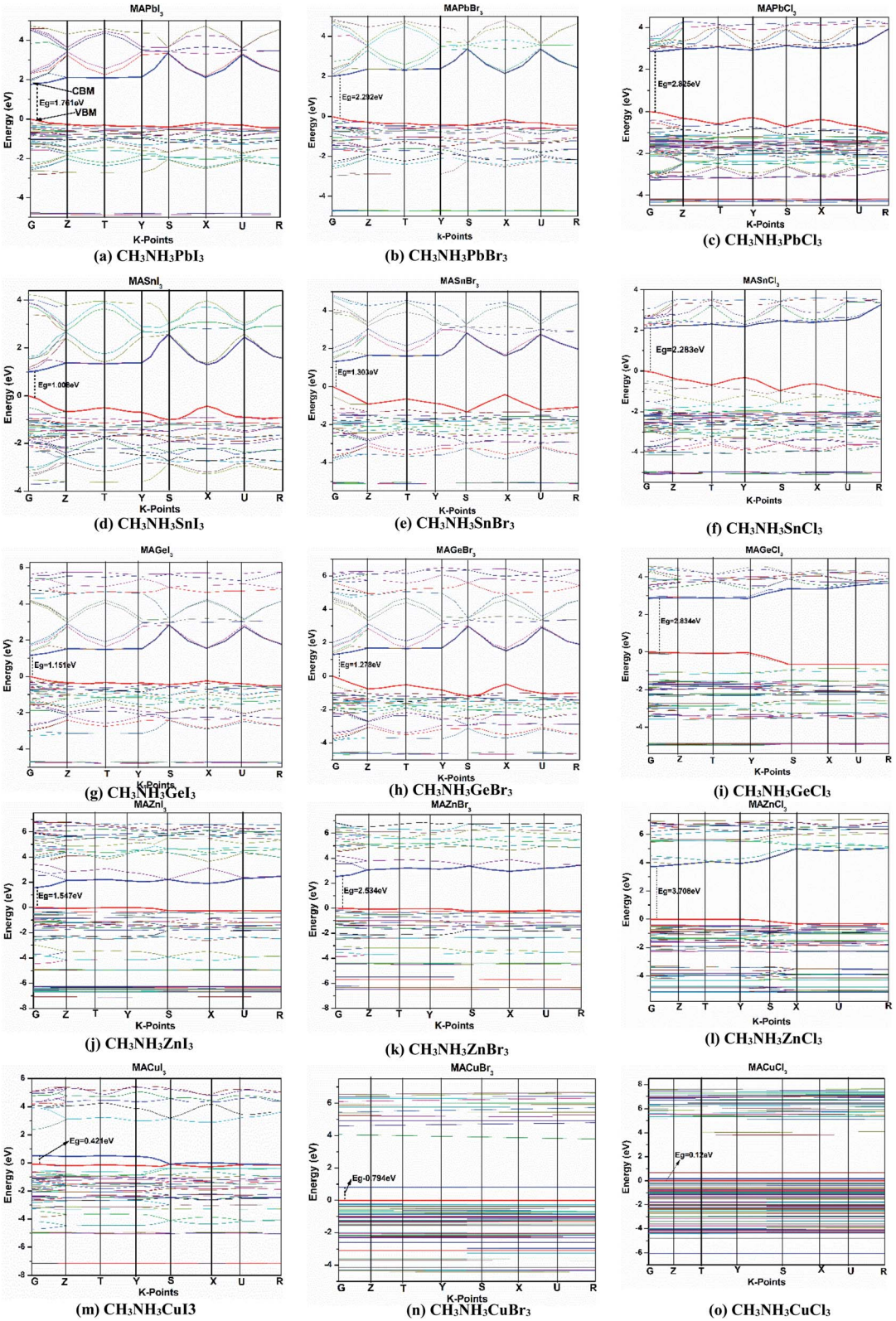

Fig. 4 Electronic energy band structures for $CH_3NH_3MX_3$ (where CH_3NH_3: MA; M: Cu, Zn, Ge, Sn, Pb; X = Cl, Br, I) in the high-symmetry direction, except for $CH_3NH_3GaX_3$ which is metallic in nature. The blue and red lines on the upper and lower sides of the Fermi level indicate the CBM and VBM, respectively.

Table 4 A list of calculated bandgaps (eV) of $CH_3NH_3MX_3$ and a comparison with available theoretical/experimental work

Material	GGA-PBE	LDA-CAPZ	Experiment/theory
$CH_3NH_3CuCl_3$	0.120	0.090	2.60 [exp.][42]
$CH_3NH_3ZnCl_3$	3.708	4.092	—
$CH_3NH_3GaCl_3$	No	No	—
$CH_3NH_3GeCl_3$	2.834	1.799	3.74–3.76 [theory][56]
$CH_3NH_3SnCl_3$	2.283	2.100	2.18 [theory],[43] 3.69 [exp.],[45] 1.94 [theory][45]
$CH_3NH_3PbCl_3$	2.825	2.334	3.1 [exp.],[57] 2.88 [theory][43]
$CH_3NH_3CuBr_3$	0.794	0.715	—
$CH_3NH_3ZnBr_3$	2.534	1.791	—
$CH_3NH_3GaBr_3$	No	No	—
$CH_3NH_3GeBr_3$	1.278	0.532	2.76–2.81 [theory][56]
$CH_3NH_3SnBr_3$	1.303	1.219	2.15, 1.04 [exp., theory][45]
$CH_3NH_3PbBr_3$	2.292	1.746	2.31, 2.26 [theory][46]
$CH_3NH_3CuI_3$	0.421	0.156	—
$CH_3NH_3ZnI_3$	1.547	0.460	—
$CH_3NH_3GaI_3$	No	No	—
$CH_3NH_3GeI_3$	1.151	0.626	1.9–2.0 [theory][56]
$CH_3NH_3SnI_3$	1.006	0.350	1.21 [exp.][21]
$CH_3NH_3PbI_3$	1.761	1.441	1.6 [exp.][1]

results. It is also noticed that the band gaps are very responsive to variation in B-site metal cations in the perovskites and they agree quite well with earlier investigations.[21,26] Moreover, the GGA functional containing the Wu–Cohen potential[59] is very effective for bandgap investigation in comparison to the results of the LDA functional (Fig. 5).[60] Bandgaps that are calculated with DFT give lower values than the experimental data but they can still be accounted for the DFT investigation.[28]

The electronic band gap can be explicated further by an investigation of the density of states (DOS). The DOS spectra of all the materials are presented in Fig. 6, which shows a comparison among them. All eighteen methylammonium metal halide perovskites possess the same type of total density of states (TDOS) except for $MAGaX_3$ where the VB crosses the Fermi level and they show metallic behavior. However, by changing the cations from Ge to Pb and Zn to Cu, the VB are shifted closer to the Fermi level, as observed in Fig. 6. The same pattern was observed for chloride, bromide and iodide perovskites. This trend is also similar to the band structures which reaffirms the study.

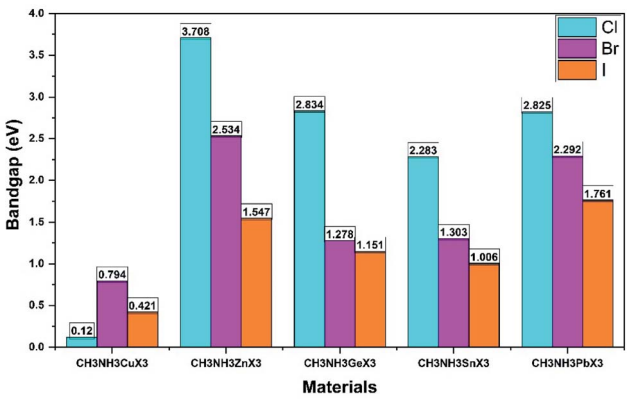

Fig. 5 An illustration of the band gap trend with a variation in the metal cation and halide anion for orthorhombic $CH_3NH_3MX_3$ (except for $CH_3NH_3GaX_3$ which is metallic in nature) using the DFT-GGA level of theory.

We have further studied the partial/projected density of state (PDOS) of our calculated perovskite compounds, which are shown in Fig. 7. In terms of atomic viewpoint, the main contribution in VB and CB comes from the M-site and X-site atoms and it causes a reduction in band gap of these compounds. The valence electrons of Ge, Sn and Pb are $4s^2\ 3d^{10}\ 4p^2$, $5s^2\ 4d^{10}\ 5p^2$ and $6s^2\ 5d^{10}\ 6p^2$, respectively. From Fig. 7, it can be noted that the PDOS of these valence electrons, especially lone-pair electrons, give the main contribution to the formation of total DOS. For heavy atoms, the energy of the valence lone pair s orbital increases with an increase in metal cation size[61,62] in the same period and in the same group which helps to make them defect-tolerant compounds. In the same-group compounds ($CH_3NH_3GeX_3$, $CH_3NH_3SnX_3$, $CH_3NH_3PbX_3$), the main contribution in the conduction band minima (CBM) comes from the partially filled $4p^2$, $5p^2$ and $6p^2$ states of the metal atom, respectively. As the d-orbital is fully filled, its contribution is quite small for this group of perovskites.

Mainly the p-orbital and partially the lone-pair s-orbital of the metal atom (lone-pair s–p hybridization) are responsible for the configuration of the CBM. Thus it increases the band gap from Ge to Pb which provided validation of the study. The VBM is dominantly formed by the valence p-orbital of the halide anion and the lone-pair s-orbitals of the metal cation make a partial contribution for these same-group compounds. The lone-pair s–p hybridization of the metal cation and halide anion are greatly related to their band gap and these will lead to making them defect-tolerant compounds, able to tune their electronic attractiveness. The band gap is also linked with the M–X bond lengths of the same-group perovskite compounds and any alteration in the material configuration or bond length of these compounds can alter the band gap. So this elucidates the cause of the reduction in band gap value from $CH_3NH_3PbX_3$ to $CH_3NH_3GeX_3$.

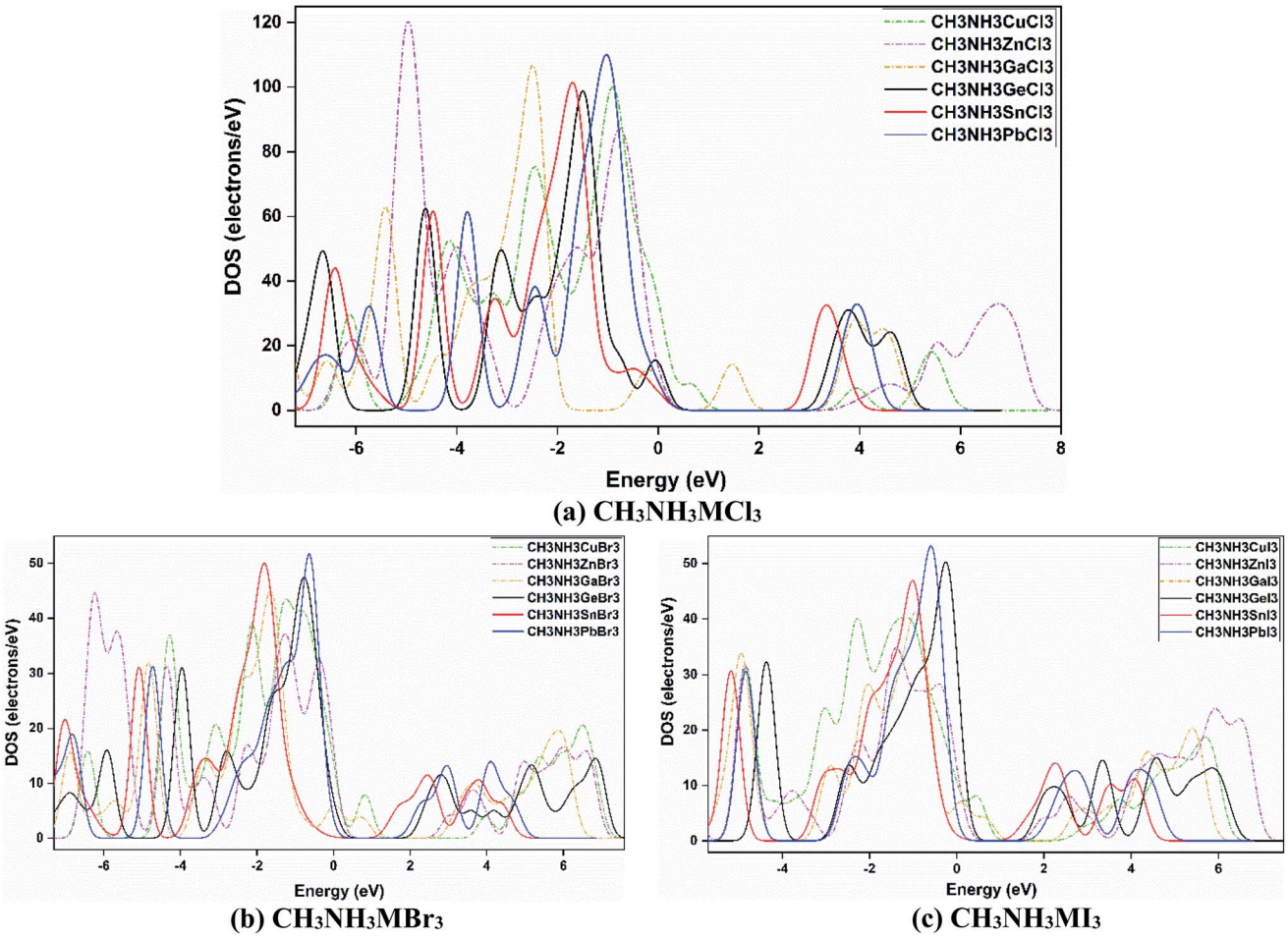

Fig. 6 Density of states (DOS) spectra for (a) $CH_3NH_3MCl_3$, (b) $CH_3NH_3MBr_3$, and (c) $CH_3NH_3MI_3$, and a comparison upon varying the metal and halide atoms in those $CH_3NH_3MX_3$ compounds.

Again in the same-period compounds ($CH_3NH_3CuX_3$, $CH_3NH_3ZnX_3$, $CH_3NH_3GaX_3$), the valence electrons of Cu, Zn and Ga are $4s^1\ 3d^{10}$, $4s^2\ 3d^{10}$ and $4s^2\ 3d^{10}\ 4p^1$, respectively. As Cu has a half-filled s-orbital, this affects the TDOS more than for Zn and Ga. Besides the Cu-d orbital contributes mainly to forming the VB near the Fermi level in the $CH_3NH_3CuX_3$ compounds. In the Cu-group compounds, the valence p-orbital and partial s-orbital of the halogen (X) anion contribute mainly to the VBM. While the main contribution of CBM comes from the s and p orbitals of the metal cation. Thus with an increase in atomic size in the same period (from Cu to Zn), the band gap increases from $CH_3NH_3CuI_3$ (0.421) to $CH_3NH_3ZnI_3$ (1.547) and similarly for other halides. Besides, the organic methylammonium part of those perovskite compounds has little impact on the CBM or VBM. Overall, organic CH_3NH_3 did not participate in the band structure; instead it contributed to the structural cohesion. Here it needs to be mentioned that as we make variations in the metal, the outer shell electrons and lone-pair s–p hybridization are changed and so is their participation in the TDOS as we go from Ge → Sn → Pb and Cu → Zn → Ga.

The coupling between the methylammonium cation (organic) and the M–X bond (inorganic) was further inspected with plots of electron charge density. They appear in ESI (Fig. S1†). For a better understanding, we present part of that depiction in Fig. 8 for $CH_3NH_3MI_3$. Here field representation has been used for plotting electron charge density. According to Fig. 8, we did not observe any electron orbital overlap between the CH_3NH_3 part and the inorganic M–X bond, which represents a weak coupling between them. So there exists ionic bonding between the organic and inorganic parts. These perceptions indicate the character of the organic molecule for balancing the charge. This also clarifies that bonding between CH_3NH_3 and M–X is ionic. In this sense, the charges in the metal halide $CH_3NH_3MX_3$ would show better transport performance.

3.3 Optical properties

Hybrid perovskite compounds become very promising as brilliant light harvesters in photovoltaics because of their organic (CH_3NH_3) part, which possesses greater optical absorption. Therefore, these compounds receive huge interest in the research community for building more efficient and effective photovoltaic and optoelectronic devices.

The optical absorption coefficient of a material is an important parameter that measures the dispersion of light at

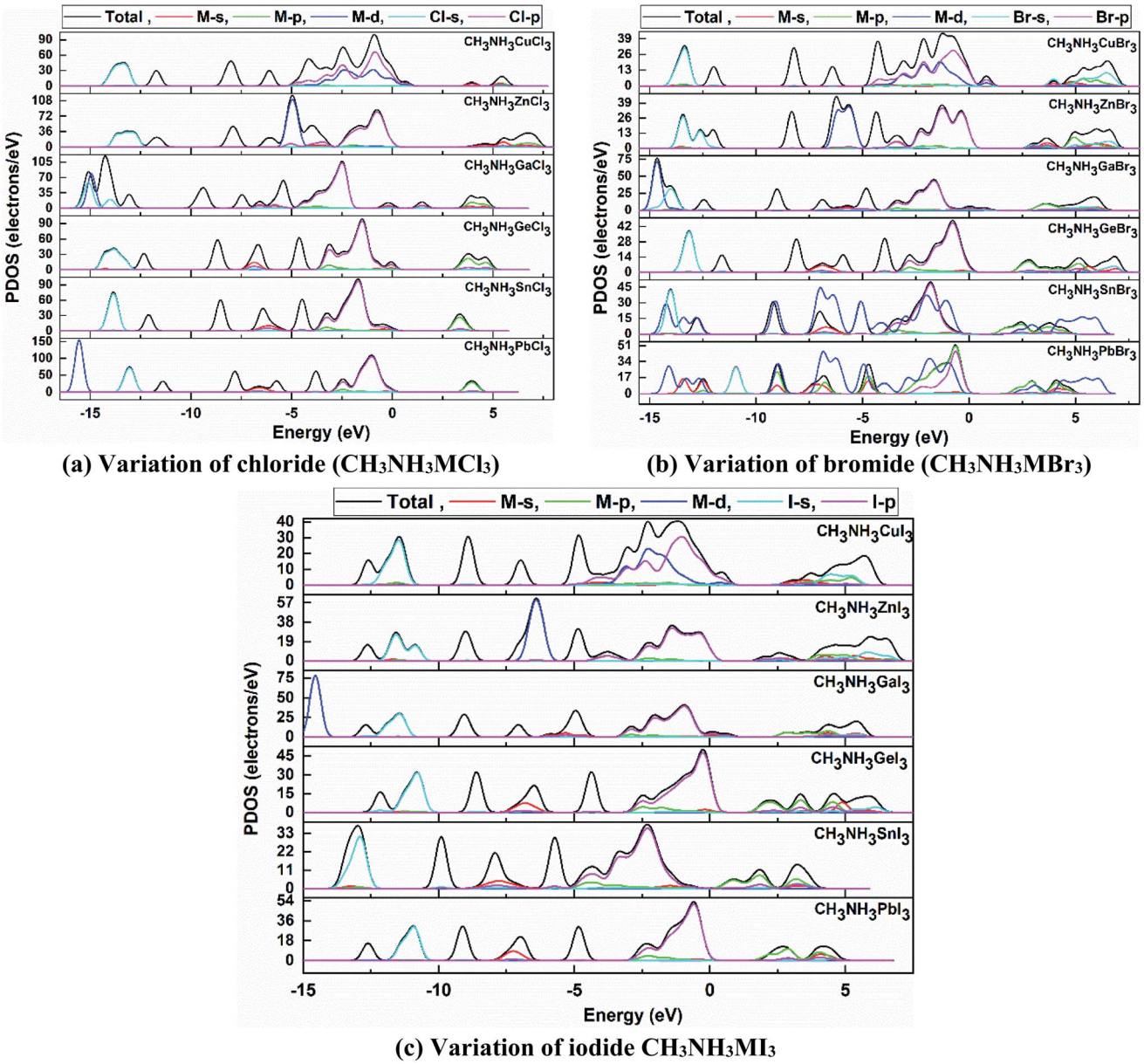

Fig. 7 Partial density of states (PDOS) plots of orthorhombic (a) $CH_3NH_3MCl_3$, (b) $CH_3NH_3MBr_3$, and (c) $CH_3NH_3MI_3$ compounds, where the dotted line represents the Fermi level at 0 K.

particular wavelengths before it becomes absorbed.[9,21] This is very helpful for providing information related to solar energy conversion efficiency. Thus, this is very relevant for the practical application of a material in photovoltaics.

In Fig. 9, optical absorption coefficient spectra of all eighteen perovskite materials are depicted. For same-group compounds ($CH_3NH_3GeX_3$, $CH_3NH_3SnX_3$, $CH_3NH_3PbX_3$), the peaks of the absorption spectra shift to (right) high energy with the variation in metal from Ge to Pb and also with the changes in halogen from Cl to I. The peak of the absorption spectra was wide for Pb iodide and Sn iodide compounds with a very wide absorption range from far UV to the visible range (174–800 nm) and another peak with a strong absorption coefficient was at 180 nm for the Ge iodide compound. In other words, all the same-group materials within this range possess durable absorption and low electron loss. So it should be pointed that all these same-group compounds were fully transparent in the visible range. Also in going from iodide to chloride compounds, the absorption range decreases gradually from the visible spectrum to near UV. On the other hand, in the same-period compounds ($CH_3NH_3CuX_3$, $CH_3NH_3ZnX_3$, $CH_3NH_3GaX_3$), the peak value shifts to higher energy when Cu is replaced with Zn or Ga, while we observe blue shifts for halogen variation from I to Cl with the total energy range between 125 and 800 nm. Besides, with the decrease in band gap, the absorption spectra of all the perovskites shift to lower energy from Pb to Ge and Ga to Cu in the iodide, bromide and chloride compounds. An exception was observed for $CH_3NH_3GaBr_3$ and $CH_3NH_3CuCl_3$ compounds

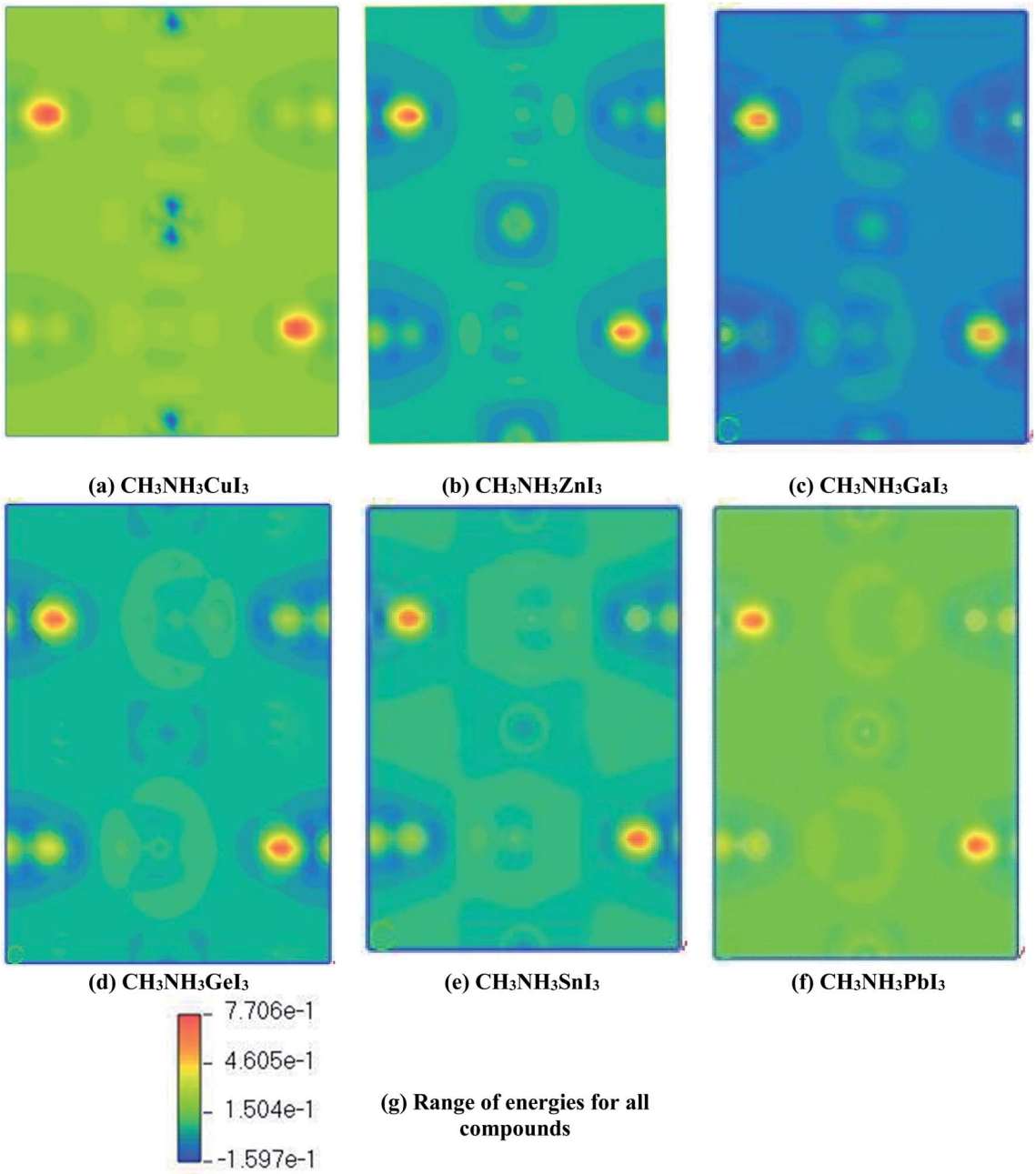

Fig. 8 Total electronic charge density for methylammonium metal iodide: a field representation. The units are electrons $Å^{-3}$. In the field representation, colors from blue to orange symbolize the change in electron density from low to high.

which absorb light over a very wide range (115–800 nm) that make them favorable candidates for diverse optoelectronic devices. Thus optical absorption has a close relationship with electronic structure. As these perovskite compounds absorb UV-Vis light, these types of material show advantages for their application in solar cells as well as in many optical and electronic applications.

Other optical properties, including reflectivity, refractive index, complex dielectric function, energy loss function and optical conductivity, of these orthorhombic perovskites have been calculated and are attached in the ESI (Fig. S2†). The zero frequency limit of dielectric function $\varepsilon_1(\omega)$, reflectivity $R(\omega)$ and refractive index $n(\omega)$ are listed in Table 5. The frequency-dependent real part of the dielectric function, $\varepsilon_1(\omega)$, is shown in Fig. S2.† From the dielectric spectra, we noticed that the compounds move to lower energy when the B-site metal atom changes from Pb to Ge and from Ga to Cu in iodide, bromide and chloride compounds (see Fig. S2†). In these spectra, we noticed a significant quantity which is the zero frequency limit $\varepsilon_1(0)$. It is considered to be a static dielectric constant. In the spectra the most important quantity is the zero frequency limit $\varepsilon_1(0)$, which is the electronic part of the static dielectric constant. The values of static $\varepsilon_1(0)$ are tabulated in Table 5. From Table 5, it is clear that for the same-group compounds,

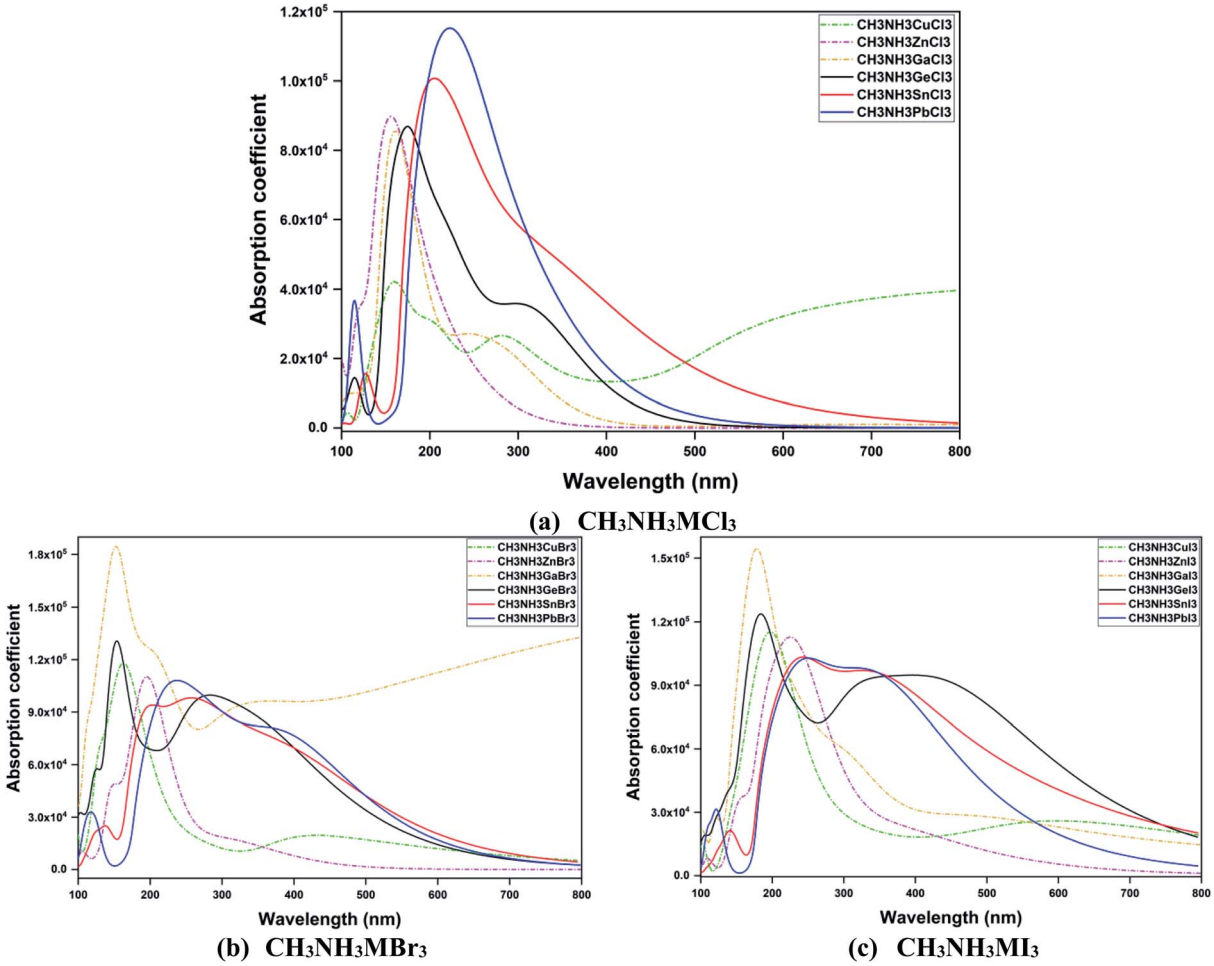

Fig. 9 A comparison of the absorption coefficient $\alpha(\omega)$ as a function of wavelength (nm) for orthorhombic $CH_3NH_3MX_3$ compounds.

Table 5 Zero frequency limit of $\varepsilon_1(\omega)$, $R(\omega)$, and $n(\omega)$ for orthorhombic $CH_3NH_3MX_3$ (M = Pb, Sn, Ge, Ga, Zn, Cu; X = I, Br, Cl)

	Parameters		
Materials	$\varepsilon_1(0)$	$R(0)$	$n(0)$
$CH_3NH_3CuCl_3$	60.156	0.661	7.860
$CH_3NH_3ZnCl_3$	1.613	0.014	1.270
$CH_3NH_3GaCl_3$	1.658	0.016	1.288
$CH_3NH_3GeCl_3$	1.951	0.027	1.397
$CH_3NH_3SnCl_3$	4.389	0.125	2.095
$CH_3NH_3PbCl_3$	2.430	0.048	1.559
$CH_3NH_3CuBr_3$	2.591	0.055	1.610
$CH_3NH_3ZnBr_3$	1.885	0.025	1.373
$CH_3NH_3GaBr_3$	791.070	0.874	28.624
$CH_3NH_3GeBr_3$	4.416	0.126	2.102
$CH_3NH_3SnBr_3$	4.159	0.117	2.039
$CH_3NH_3PbBr_3$	4.041	0.113	2.010
$CH_3NH_3CuI_3$	5.077	0.149	2.254
$CH_3NH_3ZnI_3$	2.586	0.054	1.608
$CH_3NH_3GaI_3$	11.279	0.299	3.375
$CH_3NH_3GeI_3$	6.832	0.199	2.614
$CH_3NH_3SnI_3$	6.688	0.196	2.586
$CH_3NH_3PbI_3$	4.26	0.121	2.064

$\varepsilon_1(0)$ decreases from Ge to Pb and increases for chloride to iodide compounds except for $CH_3NH_3GeCl_3$. This shows that bandgap and $\varepsilon_1(0)$ share an inverse relationship. For same-period compounds the value of $\varepsilon_1(0)$ decreases from Cu to Zn and increases from Zn to Ga based compounds. Also with the variation in halide (from I to Cl), the value of $\varepsilon_1(0)$ decreases, with the exception of $CH_3NH_3GaBr_3$ ($\approx$791 eV) and $CH_3NH_3CuCl_3$ ($\approx$60 eV). These values are unusually high and they also absorb light over a very wide range, as depicted in Fig. 9. This makes these two materials interesting in various optoelectronic device applications.

It is also noted that $R(0)$ shows similar behavior to $\varepsilon_1(0)$ in both categories (same group and same period) of compound and also with iodide to chloride compounds. Similar exceptions occurred for $CH_3NH_3GeCl_3$, $CH_3NH_3GaBr_3$ and $CH_3NH_3CuCl_3$. The highest $R(0)$ value was noted for $CH_3NH_3GaBr_3$ (0.874 eV) which also possesses a very high dielectric function (791 eV). The zero frequency refractive index $n(0)$ further shows analogous behavior to $\varepsilon_1(0)$ in both categories of compound and also in iodide to chloride compounds.

For same-group compounds, $CH_3NH_3SnCl_3$ is an exception in $n(0)$ while $CH_3NH_3GaBr_3$ and $CH_3NH_3CuCl_3$ are exceptions for same-period compounds. The infrequent high refractive

index of $CH_3NH_3GaBr_3$ (28.624) and $CH_3NH_3CuCl_3$ (7.860) is far greater than the value for diamond, the natural material with the highest refractive index. Thus $CH_3NH_3GaBr_3$ and $CH_3NH_3CuCl_3$ can be turned into artificial and unusual jewel crystals. If the value of the refractive index falls below unity (see Fig. S2†) then it can be able to absorb X-rays, γ-rays and a percentage of UV photons which make these materials superluminescent for these types of rays. So these low values of refractive index ($n = c/V_g$) imply that V_g swings to the negative realm (as $V_g > c$) and the medium changes from linear to non-linear which is indicative of the superluminal nature of these materials ($CH_3NH_3GaBr_3$ and $CH_3NH_3CuCl_3$).

4 Conclusions

First-principles DFT calculations were performed on orthorhombic hybrid metal halide perovskites of the form $CH_3NH_3MX_3$ (M: Cu, Zn, Ga, Ge, Sn, Pb; X: Cl, Br and I) to investigate their geometric, electronic, and optical properties and to understand their atomistic origin and the effects of lone-pair orbitals (s–p hybridization) upon varying the metal cations and halogen anions in these perovskite compounds. According to the tolerance factor limit and μ, all eighteen materials may form stable 3D perovskite compounds, except $CH_3NH_3GaX_3$, which may be a non-perovskite and could be used in other optoelectronic devices. The calculated lattice parameters are directly related to the atomic radii of the metals and are entirely compatible with the experimental values. M–X bonds become more important when the size of the metal cation increases in the same group (Ge to Pb) and the same period (Cu to Ga), and the bond length changes are found to be more significant in the equatorial direction. Also, the calculated M–X bond lengths reduce upon going from I to Cl.

According to the electronic band structures, all the hybrid perovskites possess a direct band gap at the G symmetry point. The calculated band gaps of these $CH_3NH_3PbX_3$ perovskites increase from Cl to I, and they agree well with experimental data. Also, $CH_3NH_3ZnI_3$ possesses a band gap of 1.547 eV, which is comparable to $CH_3NH_3PbI_3$ (1.761 eV), making this material ($CH_3NH_3ZnI_3$) a vital candidate for lead-free solar cell applications. The VBM is mainly contributed to by the p orbital of the halide atom, the CBM comprises the lone-pair s and p orbitals of the metal atom near the Fermi level, and organic CH_3NH_3 does not contribute to the electronic structure. The impact of the hybridization of the lone-pair (ns^2) electrons of the metal cation with the halide anion (lone-pair p-orbital) leads to some unfamiliar properties being shown by these metal halide compounds, which is encouraging for optoelectronic applications. This lone-pair hybridization plays a key role in producing defect-tolerant compounds and is also responsible for suitable band alignments, making these materials perfect absorbers for visible light. Moreover, PDOS plots suggest a relationship between the band gap and the effect of the lone pair (*i.e.*, s–p hybridization) and M–X bonding. Therefore, any alteration at a metal or halogen site can easily affect the band gap values.

From the viewpoint of optical absorption spectra, all the orthorhombic perovskite materials show blue shifting from Pb to Ge and Ga to Cu in iodide, bromide, and chloride compounds. For same-group compounds ($CH_3NH_3GeX_3$, $CH_3NH_3SnX_3$, and $CH_3NH_3PbX_3$), $\varepsilon_1(0)$, $R(0)$, and $n(0)$ decrease from Ge to Pb and increase when moving from chloride to iodide compounds. Disruptive behavior has been observed for same-period compounds ($CH_3NH_3CuX_3$, $CH_3NH_3ZnX_3$, and $CH_3NH_3GaX_3$). $CH_3NH_3GaBr_3$ and $CH_3NH_3CuCl_3$ could be promising nontoxic materials for use in optoelectronic devices as they absorb a wide range of light (from far-UV to visible) and possess very unusual high dielectric functions and refractive indices.

Data availability

Data are available upon request from the authors.

Author contributions

Maliha Nishat: Software, Methodology, Formal analysis, Investigation, Writing-Original Draft Md. Rakib Hossain: Writing-Review and Editing, Visualization Md. Kamal Hossain: Conceptualization, Methodology, Validation, Data Curation, Writing-Review and Editing Shamima Khanom: Writing-Review and Editing, Visualization Farid Ahmed: Resources, Project administration, Funding acquisition Md. Abul Hossain: Visualization, Supervision.

Conflicts of interest

There are no conflicts of interest to declare.

Acknowledgements

We gratefully acknowledge the Higher Education Quality Enhancement Program (HEQEP) subproject CP-3415, University Grant Commission (UGC) of Bangladesh and the World Bank for financial assistance to set up the Computational Physics (CP) Research Lab in the Department of Physics at Jahangirnagar University.

References

1 A. Kojima, K. Teshima, Y. Shirai and T. Miyasaka, *J. Am. Chem. Soc.*, 2009, **131**, 6050–6051.
2 M. A. Green, Y. Hishikawa, E. D. Dunlop, D. H. Levi, J. Hohl-Ebinger and A. W. Y. Ho-Baillie, *Prog. Photovoltaics Res. Appl.*, 2018, **26**, 3–12.
3 W. Shockley and H. J. Queisser, *J. Appl. Phys.*, 1961, **32**, 221104–67188617.
4 H. J. Snaith, *J. Phys. Chem. Lett.*, 2013, **4**, 3623–3630.
5 Q. Dong, Y. Fang, Y. Shao, P. Mulligan, J. Qiu, L. Cao and J. Huang, *Science*, 2015, **347**, 967–970.
6 S. D. Stranks, G. E. Eperon, G. Grancini, C. Menelaou, M. J. P. Alcocer, T. Leijtens, L. M. Herz, A. Petrozza and H. J. Snaith, *Science*, 2013, **342**, 341–344.
7 W. Zhang, G. E. Eperon and H. J. Snaith, *Nat. Energy*, 2016, **1**, 16048.

8 B. R. Sutherland, S. Hoogland, M. M. Adachi, P. Kanjanaboos, C. T. O. Wong, J. J. McDowell, J. Xu, O. Voznyy, Z. Ning, A. J. Houtepen and E. H. Sargent, *Adv. Mater.*, 2015, **27**, 53–58.
9 J. Burschka, N. Pellet, S. J. Moon, R. Humphry-Baker, P. Gao, M. K. Nazeeruddin and M. Grätzel, *Nature*, 2013, **499**, 316–319.
10 J. H. Noh, S. H. Im, J. H. Heo, T. N. Mandal and S. Il Seok, *Nano Lett.*, 2013, **13**, 1764–1769.
11 T. Baikie, Y. Fang, J. M. Kadro, M. Schreyer, F. Wei, S. G. Mhaisalkar, M. Graetzel and T. J. White, *J. Mater. Chem. A*, 2013, **1**, 5628–5641.
12 Y. Dang, Y. Liu, Y. Sun, D. Yuan, X. Liu, W. Lu, G. Liu, H. Xia and X. Tao, *CrystEngComm*, 2015, **17**, 665–670.
13 L. Chi, I. Swainson, L. Cranswick, J. H. Her, P. Stephens and O. Knop, *J. Solid State Chem.*, 2005, **178**, 1376–1385.
14 I. P. Swainson, R. P. Hammond, C. Soullière, O. Knop and W. Massa, *J. Solid State Chem.*, 2003, 97–104.
15 F. Brivio, J. M. Frost, J. M. Skelton, A. J. Jackson, O. J. Weber, M. T. Weller, A. R. Goñi, A. M. A. Leguy, P. R. F. Barnes and A. Walsh, *Phys. Rev. B: Condens. Matter Mater. Phys.*, 2015, **92**, 144308.
16 J. Feng and B. Xiao, *J. Phys. Chem. Lett.*, 2014, **5**, 1278–1282.
17 W. Geng, L. Zhang, Y. N. Zhang, W. M. Lau and L. M. Liu, *J. Phys. Chem. C*, 2014, **118**, 19565–19571.
18 X. Zhu, H. Su, R. A. Marcus and M. E. Michel-Beyerle, *J. Phys. Chem. Lett.*, 2014, **5**, 3061–3065.
19 G. Hodes, *Science*, 2013, **342**, 317–318.
20 L. Lang, J. H. Yang, H. R. Liu, H. J. Xiang and X. G. Gong, *Phys. Lett. A*, 2014, **378**, 290–293.
21 C. C. Stoumpos, C. D. Malliakas and M. G. Kanatzidis, *Inorg. Chem.*, 2013, **52**, 9019–9038.
22 T. Ahmed, C. La-O-Vorakiat, T. Salim, Y. M. Lam, E. E. M. Chia and J. X. Zhu, *Europhys. Lett.*, 2014, **108**, 67015.
23 O. Almora, C. Aranda, E. Mas-Marzá and G. Garcia-Belmonte, *Appl. Phys. Lett.*, 2016, **109**, 173903.
24 C. C. Stoumpos, L. Frazer, D. J. Clark, Y. S. Kim, S. H. Rhim, A. J. Freeman, J. B. Ketterson, J. I. Jang and M. G. Kanatzidis, *J. Am. Chem. Soc.*, 2015, **137**, 6804–6819.
25 D. H. Fabini, R. Seshadri and M. G. Kanatzidis, *MRS Bull.*, 2020, **45**, 467–477.
26 B. Saparov and D. B. Mitzi, *Chem. Rev.*, 2016, **116**, 4558–4596.
27 R. Chen, D. Hou, C. Lu, J. Zhang, P. Liu, H. Tian, Z. Zeng, Q. Xiong, Z. Hu, Y. Zhu and L. Han, *Sustain. Energy Fuels*, 2018, **2**, 1093–1100.
28 W. Kohn and L. J. Sham, *Phys. Rev.*, 1965, **140**, A1133–A1138.
29 M. D. Segall, P. J. D. Lindan, M. J. Probert, C. J. Pickard, P. J. Hasnip, S. J. Clark and M. C. Payne, *J. Phys. Condens. Matter*, 2002, **14**, 2717–2744.
30 D. Vanderbilt, *Phys. Rev. B: Condens. Matter Mater. Phys.*, 1990, **41**, 7892–7895.
31 J. P. Perdew, K. Burke and M. Ernzerhof, *Phys. Rev. Lett.*, 1996, **77**, 3865–3868.
32 D. M. Ceperley and B. J. Alder, *Phys. Rev. Lett.*, 1980, **45**, 566–569.
33 J. P. Perdew and A. Zunger, *Phys. Rev. B: Condens. Matter Mater. Phys.*, 1981, **23**, 5048–5079.
34 H. J. Monkhorst and J. D. Pack, *Phys. Rev. B: Condens. Matter Mater. Phys.*, 1976, **13**, 5188–5192.
35 A. S. Thind, X. Huang and R. Mishra, *Chem. Mater.*, 2009, **29**, 6003–6011.
36 S. Sun and A. K. C. Gregor Kieslich, *Chem. Sci.*, 2015, **6**, 3430–3433.
37 R. D. Shannon, *Acta Crystallogr. A*, 1976, **32**, 751–767.
38 S. Sun and A. K. C. Gregor Kieslich, *Chem. Sci.*, 2014, **5**, 4712–4715.
39 M. A. Green, A. Ho-Baillie and H. J. Snaith, *Nat. Photonics*, 2014, **8**, 506–514.
40 M. Becker, T. Klüner and M. Wark, *Dalton Trans.*, 2017, **46**, 3500–3509.
41 C. Li, X. Lu, W. Ding, L. Feng, Y. Gao and Z. Guo, *Acta Crystallogr. Sect. B Struct. Sci.*, 2008, **64**, 702–707.
42 S. S. Ashrafi, K. Hossain, F. Ahmed, A. Hossain and O. Rahman, *Adv. Mater. Phys. Chem.*, 2020, **10**, 1–16.
43 E. Mosconi, P. Umari and F. De Angelis, *Phys. Chem. Chem. Phys.*, 2016, **18**, 27158–27164.
44 A. Poglitsch and D. Weber, *J. Chem. Phys.*, 1987, **87**, 6373–6378.
45 F. Chiarella, A. Zappettini, F. Licci, I. Borriello, G. Cantele, D. Ninno, A. Cassinese and R. Vaglio, *Phys. Rev. B: Condens. Matter Mater. Phys.*, 2008, **77**, 045129.
46 Z. Yi and Z. Fang, *J. Phys. Chem. Solids*, 2017, **110**, 145–151.
47 J. Feng and B. Xiao, *J. Phys. Chem. C*, 2014, **118**, 19655–19660.
48 M. T. Weller, O. J. Weber, P. F. Henry, A. M. Di Pumpo and T. C. Hansen, *Chem. Commun.*, 2015, **51**, 4180–4183.
49 Y. Wang, T. Gould, J. F. Dobson, H. Zhang, H. Yang, X. Yao and H. Zhao, *Phys. Chem. Chem. Phys.*, 2014, **16**, 1424–1429.
50 D. A. Egger and L. Kronik, *J. Phys. Chem. Lett.*, 2014, **5**, 2728–2733.
51 Y. Pan, S. Chen and Y. Jia, *Int. J. Hydrogen Energy*, 2020, **45**, 6207–6216.
52 Y. Pan, *Vacuum*, 2020, **181**, 109742.
53 I. L. Ivanov, A. S. Steparuk, M. S. Bolyachkina, D. S. Tsvetkov, A. P. Safronov and A. Y. Zuev, *J. Chem. Thermodyn.*, 2018, **116**, 253–258.
54 A. Senocrate, G. Y. Kim, M. Grätzel and J. Maier, *ACS Energy Lett.*, 2019, **4**, 2859–2870.
55 A. Walsh and G. W. Watson, *J. Solid State Chem.*, 2005, **178**, 1422–1428.
56 S. F. Hoefler and G. Trimmel, *Monatsh. Chem.*, 2017, **148**, 795–826.
57 G. C. Papavassiliou and I. B. Koutselas, *Synth. Met.*, 1995, **71**, 1713–1714.
58 H. Zhou, Q. Chen, G. Li, S. Luo, T. Song, H.-S. Duan, Z. Hong, J. You, Y. Liu and Y. Yang, *Science*, 2014, **345**, 542–546.
59 Z. Wu and R. E. Cohen, *Phys. Rev. B: Condens. Matter Mater. Phys.*, 2006, **73**, 2–7.
60 B. G. Chae, D. H. Youn, H. T. Kim, S. Y. Maeng and K. Y. Kang, *J. Korean Phys. Soc.*, 2003, **44**, 884–888.
61 A. Walsh, D. J. Payne, R. G. Egdell and G. W. Watson, *Chem. Soc. Rev.*, 2011, **40**, 4455–4463.
62 Z. Xiao, K. Z. Du, W. Meng, J. Wang, D. B. Mitzi and Y. Yan, *J. Am. Chem. Soc.*, 2017, **139**, 6054–6057.